Original article

Experimental study on the isothermal adsorption of methane gas in natural gas hydrate argillaceous silt reservoir

Rongrong Qi[1,2], Xuwen Qin[1,3], Cheng Lu[4,5]*, Chao Ma[1,2], Wenjing Mao[1,2], Wentong Zhang[6]

[1]*Southern Marine Science and Engineering Guangdong Laboratory (Guangzhou), Guangzhou 511458, P. R. China*

[2]*Guangzhou Marine Geological Survey, China Geological Survey, Guangzhou 510075, P. R. China*

[3]*China Geological Survey, Beijing 100083, P. R. China*

[4]*Oil and Gas Resource Survey Center, China Geological Survey, Beijing 100083, P. R. China*

[5]*School of Energy Resources, China University of Geosciences, Beijing 100083, P. R. China*

[6]*Department of Chemistry, Faculty of Science, University of Alberta, Edmonton, Alberta T6G2G2, Canada*

Abstract:
Gas hydrate occurs in hydrate reservoirs in a solid form. At present, the conventional exploitation method is to decompose solid hydrate and then extract the resulting gaseous gas. Therefore, the occurrence law of gas in a reservoir is of great significance for the study of gas hydrate seepage and productivity. Adsorption, as an important occurrence mode, has been widely concerned in the research on shale reservoirs. However, the adsorption problem in hydrate reservoirs has not received enough attention. In this paper, the existence of adsorption in a hydrate reservoir has been experimentally confirmed for the first time. Based on the argillaceous silt of a natural gas hydrate reservoir in the South China Sea, the pore structure and adsorption characteristics of argillaceous silt were experimentally studied, and the results were compared with those of typical shale reservoirs. The modified Langmuir and Dubinin-Radushevich equations were used to fit the adsorption data, and the suitable adsorption model of argillaceous silt was established and optimized. The results showed that the inhomogeneous slit pores are dominant in argillaceous silt, and they are formed by the accumulation of lamellar particles. Compared with shale, the adsorption capacity of argillaceous silt is weak under the same conditions. However, adsorption is a spontaneous exothermic reaction, and the ambient temperature of argillaceous silt is much lower than that of shale. Therefore, it is possible for argillaceous silt to achieve an adsorption capacity comparable to that of shale. The modified Langmuir model can be used to simulate argillaceous silt adsorption at low pressure, while under medium and high pressures, the modified Dubinin-Radushevich model performs better. The adsorption capacity of argillaceous silt is affected by moisture. When the water content is 20%, the Langmuir adsorption capacity and the Dubinin-Radushevich maximum adsorption capacity decreases by 21.88% and 13.67%, respectively, which is far less than the influence of moisture on shale adsorption, as reported in the literature.

1. Introduction

Natural gas hydrate (NGH), an ice-like cage crystalline substance formed by gas molecules and water under the conditions of low temperature and high pressure, is mainly distributed in the continental margin of oceans and high-latitude tundra. NGH is known as a potential alternative energy source of the 21st century due to its large reserves, wide distribution and high energy density (Liu et al., 2015; Li et al., 2018; Qin et al., 2020; Ye et al., 2020; Shaibu et al., 2021). The total carbon content of global NGH resources is estimated to be about 180 billion tons, more than twice the total amount of conventional fossil energy, while marine NGH resources account for more than 95% of the total amount of hydrate

resources (Ruppel and Kessler, 2016).

The basic idea of gas hydrate exploitation is to decompose gas hydrate in situ to produce natural gas and water by changing the phase equilibrium conditions, and then transport natural gas to the ground along pores, natural cracks, artificial cracks and pipe strings, so as to achieve the efficient exploitation of hydrate. Adsorption refers to the suction phenomenon of the gas or liquid to a solid surface, which is mainly divided into chemical adsorption and physical adsorption processes. Chemical adsorption relies on the chemical bond between adsorbed gas and solid surface, which is selective and irreversible, while physical adsorption is related to van der Waals force, which is reversible and non-selective (Mohammadi et al., 2021). Generally speaking, the adsorption of natural gas on rock occurs through physical adsorption (Busch and Gensterblum, 2011). The concept of "adsorption" is frequently mentioned in relation to organic-rich shale reservoirs, mainly because large amounts of gases are deposited on the inner surface of organic matter and clay minerals or dissolved in organic matter (Zhu et al., 2020; Liu et al., 2021a, 2021b). As the mineral composition of NGH reservoirs is similar to shale (Ji et al., 2012; Liu et al., 2015), and they feature a large number of micro-/nanopores, there may be a certain adsorption effect during hydrate exploitation. Adsorption is a function of pressure; as the pressure decreases, the adsorbed gas is desorbed into free gas, which can supplement the gas production. Conversely, the gas may be partially reabsorbed into the reservoir pores during flow, which in turn reduces gas production. Therefore, it is of great significance to study the adsorption characteristics of methane gas in NGH reservoirs for the estimation of gas reserves, the judgment of gas exploitation timing, and the gas flow in such reservoirs.

Among the factors affecting shale adsorption, organic matter content is the most important one; the higher its content, the stronger the adsorption capacity of shale (Ross and Bustin, 2007, 2009; Zhu et al., 2018; Qi et al., 2018, 2019). In addition, the influence of shale mineral composition and pore structure on adsorption cannot be ignored. The adsorption capacity of different clay minerals under the same conditions is ranked as follows: montmorillonite≥illite/smectite mixed layer>kaolinite>chlorite>illite (Ji et al., 2012); the larger the pore volume and specific surface area of shale, the greater its adsorption capacity (Li et al., 2015; Zhou et al., 2018). There is a certain amount of water in shale reservoirs (Shen et al., 2019). For a long time, scholars have carried out a series of studies on the distribution of water in pores, as well as on the competitive adsorption of water and methane. Studies by Chalmers and Bustin (2007) indicated that water is mainly located in organic micropores. Compared with dry shale samples, the adsorption capacity of moist shale samples (water content: 0.44%~2.52%) decreased by 19.7%~36.1%, and the main competitive sites of methane and water were distributed in the pores of about 2~7 nm (Wang and Yu, 2016). The decrease of methane adsorption capacity is linearly correlated with the increase of water content until the critical threshold of 0.6~1 mmol/g (relative humidity 50%~75%) is reached, and the increase of water content has no further influence on adsorption (Merkel et al., 2015). Adsorption

is a spontaneous exothermic reaction. With the increase of temperature, the adsorbed amount gradually decreases. The relationship between the maximum adsorption amount and temperature can be described by a linear model (Rexer et al., 2013).

Unlike shale gas reservoirs, NGH reservoirs do not contain organic matter, but their mineral composition is similar to shale. Through X-ray diffraction (XRD) mineral composition analysis, it was shown that argillaceous silt reservoirs in the South China Sea contain about 54.4% carbonate minerals, 22% clay minerals, 17.2% quartz, and 6.3% feldspar. The main component of carbonate minerals is aragonite (46.6%), and that of clay minerals is illite (20.59%) (Liu et al., 2015). Although organic matter is considered as the main contributor to adsorption in shale gas reservoirs, the involvement of clay minerals in the adsorption process is also generally accepted. Liu et al. (2013) carried out methane isothermal adsorption experiments on montmorillonite, kaolinite and illite under the conditions of 60 °C and maximum pressure of 18 MPa, and the Langmuir adsorption capacity of montmorillonite, kaolinite and illite could reach 6.01 cm^3/g, 3.88 cm^3/g and 2.22 cm^3/g, respectively. Gasparik et al. (2012) showed that the methane adsorption capacity of low-TOC and clay-rich shale was equal to or even higher than that of organic-rich shale, and the maximum Langmuir adsorption capacity was positively correlated with clay content. Schettler and Parmely (1991) found higher adsorption capacity in low-TOC shales, which the researchers attributed to the adsorption properties of clay minerals, especially of illite. They carried out adsorption tests on pure illite and montmorillonite, and demonstrated that pure clay minerals have a methane adsorption capacity that is comparable to organic-rich shales. Lu et al. (1995) also indicated that the adsorption amount of methane on illite was considerable. However, Ross and Bustin (2009) pointed out that clay minerals do not contribute to gas adsorption when water is present due to their hydrophilic properties, that is, water blocks the passage of gas molecules to adsorption sites. In addition, because adsorption is a spontaneous exothermic reaction, it is more likely to occur at a lower temperature, and the temperature of NGH reservoir is much lower than that of shale reservoir, making it possible for a NGH reservoir to have an adsorption amount comparable to that of shale reservoirs. Therefore, it is necessary to explore the adsorption characteristics of argillaceous silt, which is of great significance to the efficient exploitation of NGH.

In this paper, low-pressure CO_2 and N_2 adsorption experiments and high-pressure methane adsorption experiments were carried out using argillaceous silt from a NGH reservoir in the South China Sea. Then, the microscopic pore structure and methane adsorption characteristics of argillaceous silt were obtained. Finally, the methane adsorption model of argillaceous silt was optimized, and the key adsorption parameters were acquired, which provides data support and theoretical guidance for subsequent research work.
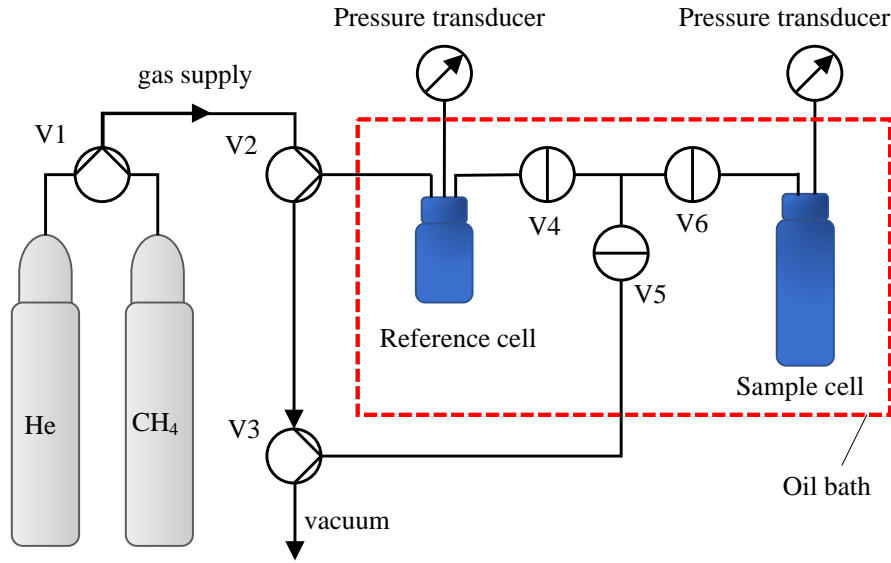
2. Experiments

2.1 Materials

Fig. 1. Schematic diagram of gas isothermal adsorption experimental device.

The samples utilized in this paper were argillaceous silt from a NGH reservoir taken from the South China Sea. For comparison, shale data from the Wufeng and Longmaxi formations in the Sichuan Basin were cited. Both the argillaceous silt and shale mentioned in this paper are mainly composed of quartz, carbonate and clay minerals. The average contents of the three minerals were 33.1%, 26.4% and 34.7% for argillaceous silt, and 63.2%, 12.7% and 22.3% for shale, respectively (Qi, 2019). For the argillaceous silt samples, methane isothermal adsorption experiments were carried out under both dry and moist conditions. Before the experiment was carried out, the samples were firstly dried for 12 hours in an 80 °C thermostat, and then ground to powder with a particle size of less than 80 mesh (0.18 mm). In order to restore the water content of hydrate reservoir under laboratory conditions, two physical parameters of water saturation and moisture content are converted in this paper, where water saturation refers to water volume in a certain pore volume, and the definition is as follows:

$$S_w = \frac{V_w}{V_b \phi} \times 100\% = \frac{m_w \rho_b}{\rho_w m_b \phi} \times 100\% \tag{1}$$

where S_w is water saturation, %; V_w represents the volume of water, cm^3; V_b refers to the sample apparent volume, cm^3; ϕ denotes porosity; m_w stands for the mass of water, g; ρ_w refers to the density of water, g/cm^3; m_b is the sample mass, g; ρ_b represents the apparent density of sample, g/cm^3.

Moisture content refers to the ratio of the mass of water in the moist sample to the mass of the dry sample:

$$m_c = \frac{m_w}{m_b} \times 100\% \tag{2}$$

where m_c refers to the moisture content, %.

By combining Eqs. (1)-(2), the relationship between water content and water saturation can be obtained as follows:

$$m_c = \frac{\rho_w \phi S_w}{\rho_b} \tag{3}$$

In the above formula, when water density, sample apparent density, porosity, and hydrate saturation are assigned values of 1 g/cm^3, 2.1 g/cm^3, 0.35 and 70%, respectively, and the calculated moisture content is 5%. In addition, due to the large amount of water produced by hydrate decomposition during exploitation, the actual moisture content of the reservoir should be greater than 5%, and this value is set as 20% in this paper.

2.2 Gas adsorption

2.2.1 Low-pressure adsorption

According to the International Union of Pure and Applied Chemistry (IUPAC) classification, pores can be divided into micropores (<2 nm), mesopores (2~50 nm) and macropores (>50 nm) (Rouquerol et al., 1994). Based on the standard static volume method, this paper carried out CO$_2$ adsorption experiments at 273 K and liquid nitrogen adsorption experiments at 77 K on an ASAP2460 surface and pore size analyzer, respectively, to characterize the pore structure characteristics of argillaceous silt samples from micropore to mesopore and macropore. Before the experiment, the samples were screened to less than 100 mesh, and about 8 g powder was degassed at 110 °C and 5 μm Hg vacuum for 10 h to remove the bound and capillary water adhered to the clay mineral surface. Finally, based on the micropore filling, multilayer adsorption and capillary condensation theory, the pore structure parameters and pore size distribution of the samples were analyzed in detail, laying a foundation for the study of the isothermal adsorption characteristics of argillaceous silt samples under high-pressure conditions.

2.2.2 High-pressure adsorption

The methane isothermal adsorption experiment was carried out by the volume method, with the schematic diagram of the experimental instrument shown in Fig. 1. As can be seen from the figure, the experimental device is mainly composed of a reference cell, a sample cell and the intermediate zone.

Among them, the reference cell consists of cells between valves 2 and 4 and the pipeline between valves 4, 5 and 6, the sample cell includes cell and pipeline on the right of valve 6, and the intermediate zone is composed of the pipeline between valves 4, 5 and 6. During the experiment, the reference cell, sample cell and intermediate zone were placed into the oil bath to keep the temperature constant. The function of the intermediate zone is to gradually transfer the gas in the reference cell to the sample cell, so as to achieve a single injection of gas into the reference cell and the multiple adsorption of samples in the sample cell. The volumes of the cells were calibrated by helium adsorption. First, stainless steel balls were loaded into the sample cell, and the oil bath temperature was set as the experimental temperature. Then, a certain amount of helium was filled into the reference cell, and the initial pressure was recorded after the pressure stabilized. Finally, the reference and sample cell were connected, helium isothermically expanded into the sample cell, and the equilibrium pressure was recorded after reaching the adsorption equilibrium. The number of steel balls in the sample cell was changed and the above steps were repeated three times to obtain three groups of initial pressure and equilibrium pressure values. According to the law of mass conservation, the following equation can be obtained:

$$\rho_r V_r = \rho_e (V_r + V_s - \Delta V) \tag{4}$$

The above formula can be converted as follows:

$$\Delta V = \frac{\rho_e - \rho_r}{\rho_e} V_r + V_s \tag{5}$$

where ΔV represents the volume of steel ball, cm^3; ρ_r and ρ_e are the corresponding densities of initial pressure and equilibrium pressure, respectively, g/cm^3. The helium density was calculated according to the literature (Carty, 1973). V_r and V_s denote the volumes of reference cell and sample cell, respectively, cm^3.

Three groups of initial and equilibrium densities were calculated based on temperature, initial and equilibrium pressures, and the relationship curve between ΔV and $(\rho_e - \rho_r)/\rho_e$ was drawn. The slope of the curve was the volume of the reference cell, and the Y-axis intercept of the curve was the volume of the sample cell.

Void volume refers to the difference between sample cell and sample skeleton volume, and its calibration process is similar to that of cell volumes. According to the law of mass conservation,

$$\rho_r V_r = \rho_e (V_r + V_v) \tag{6}$$

That is,

$$V_v = \frac{\rho_e - \rho_r}{\rho_e} V_r \tag{7}$$

where V_v represents the void volume, cm^3.

During the isothermal adsorption experiment, a certain amount of methane gas is filled into the reference cell, which is the initial gas quantity of the system. By opening and closing valves 4 and 6, methane gas in the reference cell is gradually transferred to the sample cell. According to the law of mass
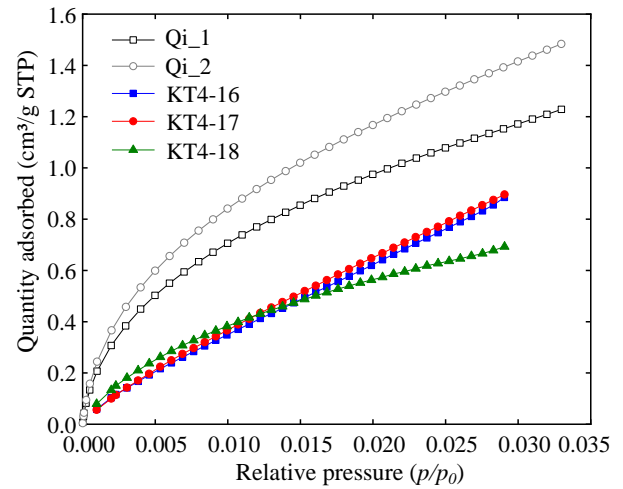

Fig. 2. Isothermal adsorption curve of CO_2 at 273 K (Qi_1 and Qi_2 are shale samples, and their data are obtained from the study of Qi (2019); KT4-16, KT4-17 and KT4-18 are the argillaceous silt samples adopted in this paper).

conservation, the methane gas adsorption capacity under different equilibrium pressures can be calculated as follows:

$$n_{ad,i} = n_{ini} - n_{r,i} - n_{e,i} = \frac{\rho_{ini}V_r - \rho_{r,i}V_r - \rho_{e,i}V_v}{M_H m_s} \times 1000 \tag{8}$$

where $n_{ad,i}$ is the methane adsorption capacity at the ith adsorption equilibrium, mmol/g; n_{ini} refers to the initial amount of gas in the reference cell, mmol/g; $n_{r,i}$ and $n_{e,i}$ respectively represent the amount of gas in the reference and sample cell at the ith adsorption equilibrium, mmol/g; ρ_{ini} is gas density at the initial pressure, g/cm^3; $\rho_{r,i}$ and $\rho_{e,i}$ are gas densities in the reference and sample cell at the ith adsorption equilibrium, respectively, g/cm^3; M_H denotes the molar mass of methane gas, g/mol; m_s is sample mass, g; for the calculation of methane gas density, refer to the literature (Setzmann and Wagner, 1991).

3. Results

3.1 Low-pressure adsorption

3.1.1 CO_2 adsorption

Fig. 2 shows the isothermal adsorption curve of CO_2 gas at 273 K. Qi_1 and Qi_2 denote shale samples of Sichuan Basin, and their data were taken from the reference (Qi, 2019). KT4-16, KT4-17 and KT4-18 are argillaceous silt samples adopted in this paper. As can be seen from the figure, for both types of samples, CO_2 adsorption capacity increases gradually with pressure, and the whole curve presents a typical type I adsorption curve. However, the adsorption capacity of argillaceous silt is lower than that of shale.

3.1.2 N_2 adsorption

Fig. 3 depicts the N_2 adsorption/desorption curves and schematic pictures of possible pore shapes for both shale and argillaceous silt. The shale samples are from Sichuan Basin, and their data are from the reference (Qi, 2019). As can be seen from the figure, in the region of low relative
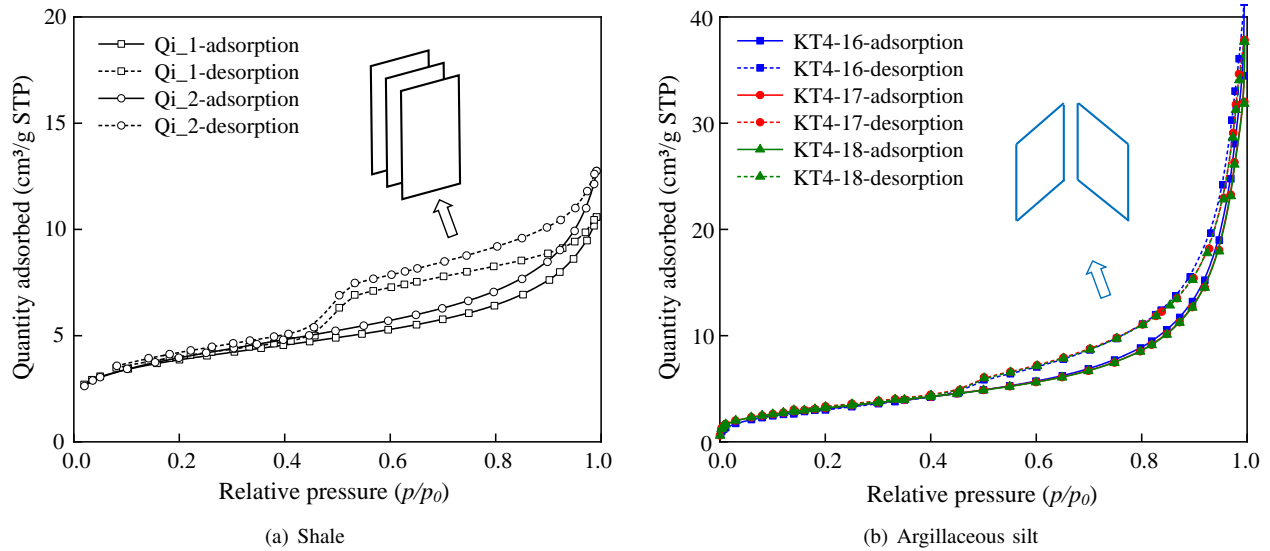
Fig. 3. N$_2$ adsorption/desorption curve and schematic illustration of possible pore shapes.

pressure ($\rho/\rho_0<0.4$), the adsorption and desorption curves almost completely coincide; at medium and high relative pressures ($\rho/\rho_0>0.4$), the adsorption and desorption curves do not coincide, and a hysteresis loop appears.

According to the IUPAC classification (Sing, 1985), the shale hysteresis loops show H4 type, indicating slit pores with uniform shape and size, and the pores are generated by layered structures (Fig. 3(a)). In such pores, capillary condensation occurs only when the pressure is close to the saturated vapor pressure, because the gas-liquid interface is nearly flat. The hysteresis loops of argillaceous silt are H3 type, indicating non-uniform slit pores, which are formed by the accumulation of lamellar particles (Fig. 3(b)). When the pressure approaches the saturated vapor pressure, capillary condensation begins to occur. Due to the pores being uneven, the Kelvin radius keeps changing, and the hysteresis loops gently decline.

3.2 High-pressure adsorption

3.2.1 Adsorption of methane on dry argillaceous silt

In this paper, the adsorption experiment of methane on argillaceous silt samples at different temperatures was carried out. The obtained adsorption curve is shown in Fig. 4. In order to determine the adsorption magnitude, the isothermal adsorption data of shale in typical regions are also listed in the figure. As can be seen from the figure, when the external conditions are similar (for example, the temperature is about 30 °C), the adsorption capacity of argillaceous silt is smaller than that of shale. This may be related to the rock composition: shale contains a certain amount of organic matter, which develops a mass of micro-/nanopores with a large specific surface area (Zhang et al., 2012). When adsorption occurs, gases preferentially enter the pores of organic matter, whose adsorption capacity per unit mass is higher than that of clay minerals. Therefore, the adsorption capacity of shale dominated by organic matter is higher than that of argillaceous silt dominated by clay minerals.
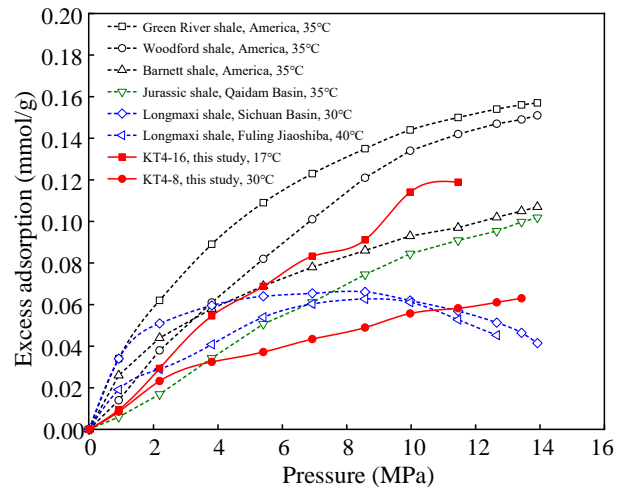

Fig. 4. Comparison of the adsorption capacities of shale and argillaceous silt under different pressures: the data for Green River Formation shale, Woodford shale and Barnett shale come from Zhang et al. (2012); the data for shale in Qaidam Basin are from Luo et al. (2015); the data for Changning shale in Sichuan Basin are obtained from Qi et al. (2018); the data for Jiaoshiba shale in Fuling are by Zhang et al. (2019).

In order to further analyze the adsorption law of argillaceous silt, this paper obtained the comparison diagram of adsorption curves between argillaceous silt and common clay minerals under dry conditions, as presented in Fig. 5. As can be seen from the figure, when the temperature is similar, the adsorption capacity of argillaceous silt sample is close to illite, which is slightly less than that of kaolinite and chlorite, and far less than that of montmorillonite.

Fig. 6 compares the isothermal adsorption curves of different argillaceous silts under dry conditions at 17 °C. As can be seen from the figure, the overall adsorption curve shows an increasing trend with pressure. When the pressure reaches a certain value, part of the adsorption curve begins to grow
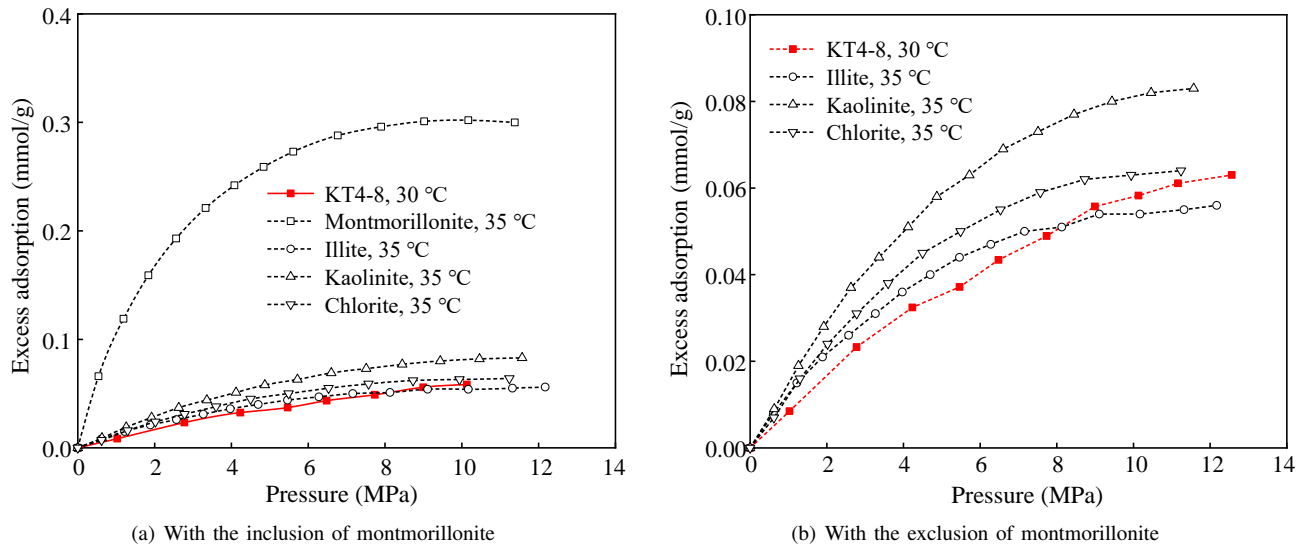
(a) With the inclusion of montmorillonite

(b) With the exclusion of montmorillonite

Fig. 5. Comparison of adsorption capacities of clay minerals and argillaceous silt under different pressures (the adsorption data of clay minerals come from Ji et al. (2012)).
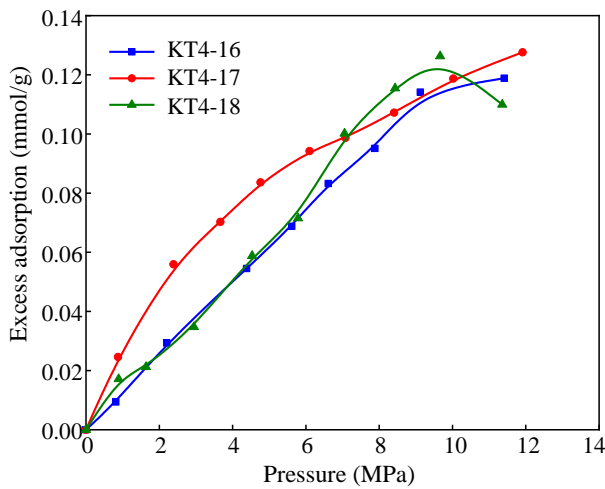

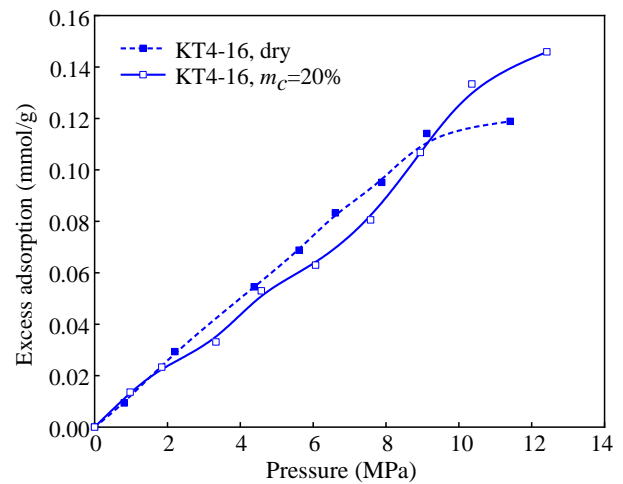**Fig. 6**. Isothermal adsorption curve of methane on argillaceous silt samples under dry conditions.

Fig. 7. Comparison of isothermal adsorption curves of argillaceous silt under dry and moist conditions.

slowly or decline.

3.2.2 Adsorption of methane on moist argillaceous silt

In order to characterize methane adsorption of argillaceous silt under moist condition, in this paper, the isothermal adsorption experiment of methane under 20% moisture content was carried out for sample KT4-16. Fig. 7 shows the isothermal adsorption curves of KT4-16 samples under dry and moist conditions at 17 °C. As can be seen from the figure, the influence of water on methane gas adsorption can be divided into three parts: At lower pressures (<2 MPa), water has almost no effect on methane adsorption; in the medium pressure range (2∼10 MPa), water reduces methane adsorption capacity as expected; at higher pressure (>10 MPa), contrary to expectations, the presence of water promotes methane adsorption.

4. Discussion

4.1 Pore structure of argillaceous silt

In order to characterize the pore characteristics of micropores in argillaceous silt, the adsorption potential theory is used to describe the experimental CO_2 adsorption data. The adsorption potential theory was put forward by Polanyi (1914). According to the theory, there is an adsorption field near the surface of the adsorbent. The space where the adsorption field acts is called the adsorption space, and there is an adsorption potential at each point in this adsorption space. Adsorption potential is a function of adsorption volume, it is independent of temperature, and is defined as the work required for 1 mol of ideal gas to compress from equilibrium pressure p_g in the gas phase to saturated vapor pressure p_0 corresponding to adsorption temperature T:

$$\varepsilon = \int_{p_g}^{p_0} V dp = \int_{p_g}^{p_0} \frac{RT}{p} dp = RT \ln \frac{p_0}{p_g} \qquad (9)$$

Subsequently, Dubinin (1966) introduced the theory of adsorption potential into the study of microporous adsorption, supposing that microporous adsorption is pore filling rather than layered adsorption. In the microporous filling process, the curve between adsorption space (i.e., filling space) and adsorption potential is a characteristic curve, which has temperature invariance. Dubinin (1966) proposed the characteristic curve equation based on a large number of experimental data, namely, the Dubinin-Radushkevich (DR) equation:

$$\theta = \frac{V}{V_0} = \exp\left[-\left(\frac{RT}{\beta E_0} \ln \frac{p_0}{p_g}\right)^2\right] \qquad (10)$$

where ε stands for adsorption potential, J/mol; θ represents the porosity filling rate, dimensionless; V is adsorption volume, cm^3/g, STP; V_0 represents the maximum adsorption volume, cm^3/g, STP; p_g stands for the pressure of the gas, MPa; p_0 is saturated vapor pressure, MPa; E_0 denotes adsorption energy, J/mol; β is the dimensionless affinity coefficient; R is the gas constant, 8.314 J/mol/K; T denotes temperature, K. In order to extend the DR equation to heterogeneous solids, Dubinin and Astakhov introduced the structure coefficient n_D, and then obtained the Dubinin-Astakhov (DA) equation (Dubinin and Astakhov, 1971):

$$\theta = \frac{V}{V_0} = \exp\left[-\left(\frac{RT}{\beta E_0} \ln \frac{p_0}{p_g}\right)^{n_D}\right] \qquad (11)$$

The gas adsorption capacity V_0 can be converted into microporous volume W_0 (cm^3/g):

$$W_0 = \frac{V_0 M_C \times 10^{-3}}{22.4 \rho_C} \qquad (12)$$

where M_C denotes the molecular weight of CO_2, 44 g/mol; ρ_C is CO_2 adsorption phase density, 1.177 g/cm^3.

In order to facilitate the comparison with N_2 BET specific surface area, the ESA (m^2/g) equivalent specific surface area of DR/DA is also calculated here:

$$ESA = \frac{V_0}{22.4 \times 10^3} N_A a_c \qquad (13)$$

where N_A is Avogadro's constant, 6.02×10^{23} mol^{-1}; a_c is the cross-sectional area of CO_2 molecule, 0.170 nm^2.

Table 1 shows the results of CO_2 microporous adsorption characterized by DR and DA equations. As can be seen from the table, the adsorption energy of CO_2 gas on shale samples is approximately equal, that is, about 23 kJ/mol (DR) and 18 kJ/mol (DA). The adsorption energies of argillaceous silt samples are 15.69~19.43 kJ/mol (DR) and 12.13~15.81 kJ/mol (DA). The adsorption energy of shale is larger than that of argillaceous silt, which explains that the CO_2 adsorption capacity of shale is larger than that of argillaceous silt under the same conditions. In addition, based on the CO_2 adsorption data, the density functional theory (DFT) was used to draw the pore size distribution curve, as shown in Fig. 8. As can be seen from the figure, the shale curves generally present two main peaks, while the argillaceous silt curves show more small peaks, indicating that the pore size distribution of argillaceous silt is more uneven.

In order to characterize the mesoporous pore structure characteristics, the BET specific surface area (BET SSA) was calculated in the relative pressure range of 0.05~0.25. According to Gurvich's rule (Gurvitsch, 1915; Marsh, 1987; Fletcher et al., 2005), the pore volume (TPV) of the sample is calculated by the adsorption amount of liquid nitrogen at a relative pressure of about 1. In this work, the average pore diameter (APD) was calculated from the known BET SSA and TPV. The Barrett-Joyner Halenda (BJH) method was used to obtain the pore size distribution of the sample (Barrett et al., 1951). The pore size distribution obtained from the N_2 desorption branch shows a false peak near 4 nm, which is ca-

Table 1. DR/DA equation fitting and calculation results.

ID	DR				
	E_0 (kJ/mol)	β	V_0 (cm^3/g, STP)	W_0 (cm^3/g)	ESA (m^2/g)
Qi_1	22.90	0.461	1.96	0.0033	8.96
Qi_2	22.42	0.461	2.44	0.0041	11.15
KT4-16	15.69	0.461	2.91	0.0049	13.30
KT4-17	15.87	0.461	2.91	0.0049	13.30
KT4-18	19.43	0.461	1.52	0.0025	6.94

ID	DA					
	E_0 (kJ/mol)	β	n_D	V_0 (cm^3/g, STP)	W_0 (cm^3/g)	ESA (m^2/g)
Qi_1	17.86	0.461	1.54	3.01	0.0050	13.75
Qi_2	17.72	0.461	1.54	3.67	0.0061	16.77
KT4-16	12.13	0.461	1.54	4.93	0.0082	22.52
KT4-17	12.30	0.461	1.54	4.88	0.0081	22.30
KT4-18	15.81	0.461	1.54	2.21	0.0037	10.09

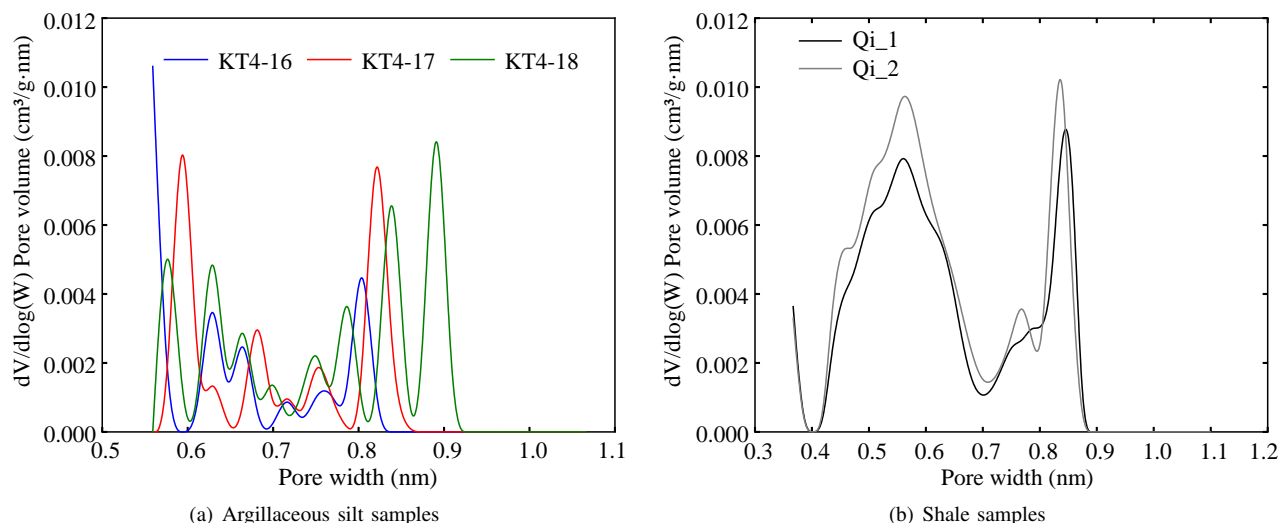(a) Argillaceous silt samples

(b) Shale samples

Fig. 8. DFT pore size distribution curve.

Table 2. Pore structure characterization results of N_2 adsorption at low temperature (the data of sample Qi_1 and Qi_2 were obtained from the literature (Qi, 2019)).

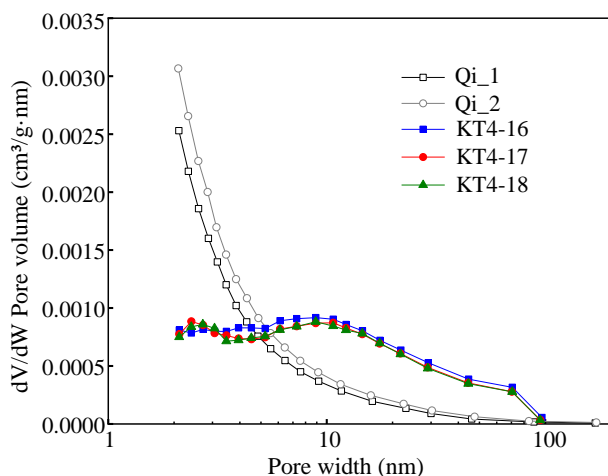| ID	BET SSA (m^2/g)	TPV (cm^3/g)	APD (nm)
Qi_1	13.86	0.016	4.72
Qi_2	14.19	0.020	5.56
KT4-16	11.89	0.059	19.85
KT4-17	11.80	0.041	13.90
KT4-18	11.77	0.040	13.59

Fig. 9. BJH pore size distribution curve (obtained from N_2 adsorption branch).

used by the tensile strength effect (Groen and Peffer, 2003), reflecting the properties of adsorbent itself rather than the pore size distribution characteristics. Therefore, the N_2 adsorption branch was selected to calculate the pore size distribution.

Table 2 presents the characterization parameters of N_2 adsorption pore structure, and Fig. 9 shows the pore size distribution curve. Compared with shale, argillaceous silt has a smaller specific surface area, while the total pore volume and average pore size are larger (Table 2). Argillaceous silt and shale samples are distributed from micropores to mesopores and macropores (Fig. 9). Among them, the proportion of micropores and mesopores in shale is high, while the distribution of pore size in argillaceous silt is uniform.

In order to better understand the difference in pore structure between argillaceous silt and shale, Table 3 lists the porosity ratios for different size ranges. As can be seen from the table, the proportion of micropores in shale is high, reaching about 60%. Meanwhile, the distribution of micropores and mesopores in argillaceous silt samples is balanced, and the proportion of mesopores is larger at about 58%.

4.2 Methane adsorption characteristics of argillaceous silt

The adsorption capacity of methane on argillaceous silt does not increase infinitely with the rise of pressure, but will reach a maximum value. The maximum value of this excess adsorption isotherm has been observed in previous supercritical adsorption studies (Myers and Monson, 2002; Zhou and Zhou, 2009; Charoensuppanimit et al., 2015). Yang et al. (2017b) attributed this phenomenon to the difference between the density of adsorbed phase and that of bulk phase. Generally speaking, the gas adsorption quantity measured under laboratory conditions constitutes the excess adsorption quantity, which is the difference between the absolute adsorption quantity and the free gas quantity in the adsorbed phase. When the pressure is low, more adsorption sites are available, and the gas density in the adsorbed phase increases rapidly, while the gas density in the free phase is relatively low, hence the adsorption capacity increases rapidly under this pressure condition. When the pressure increases to a certain value, the gas adsorption gradually approaches saturation, and the gas density in the adsorbed phase grows slowly, while the gas de-

Table 3. Pore structure characterization results of N_2 adsorption at low temperature.

ID	Micropore porosity ratio (%)	Mesopore porosity ratio (%)	Macropore porosity ratio (%)
Qi_1	61.56	29.65	8.79
Qi_2	60.91	29.84	9.26
KT4-16	38.95	58.96	2.09
KT4-17	39.21	58.75	2.04
KT4-18	39.04	58.91	2.05

Table 4. Calculation parameters of methane gas solubility in water at 45 °C.

Parameter	Unit	Value
a	MPa	5,302.07
b	-	150.4
c	1/MPa	-0.78

nsity in the free phase continues to increase, resulting in a decrease in the difference between gas density in the adsorbed phase and the free phase. Therefore, part of the adsorption curve has a downward trend under higher pressure.

According to the adsorption results of argillaceous silt under moist conditions, the adsorption effect of gas and water is not significant under low pressure; water has little influence on gas adsorption. With the increase of pressure, however, the adsorption capacity of both gas and water increases, and part of water occupies the adsorption site of gas, leading to a gradual decrease in the adsorption capacity of gas compared with dry conditions. According to the study of Yang et al. (2017a), the evolution of methane adsorption capacity with water content can be divided into three stages, namely, initial decline stage, steep decline stage and slow decline stage. In the initial decline stage, water and methane compete for adsorption on the clay mineral surface; in the steep decline stage, water molecular clusters block pore space; in the slow decline stage, water phase gathers and fills large pores. In this paper, the adsorption of methane gas and water is not significant at low and medium pressure stages, and part of the water occupies the methane adsorption sites, leading to a decrease in methane adsorption capacity. This corresponds to the initial decline stage summarized by Yang et al. (2017a).

Under high pressure, abnormal results appear under dry and moist conditions, that is, the presence of water increases the amount of gas adsorption, which may be related to the partial dissolution of methane gas in water. In order to discuss the dissolution of gas in water, the empirical formula of Chareonsuppanimit et al. (2012) was adopted to characterize the solubility of gas at different pressures:

$$x_g = \frac{p_g}{a + b p_g + c p_g^2} \tag{14}$$

where x_g refers to the solubility of the gas; a, b and c are the model parameters. As the solubility of methane in water is low, the same parameters used by Chareonsuppanimit et al.
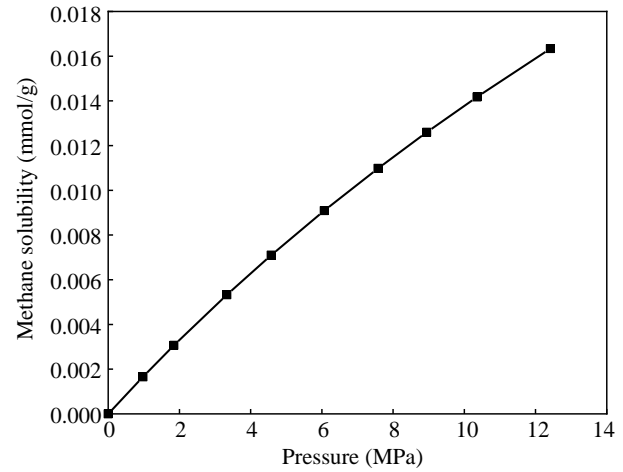

Fig. 10. Dissolution curves of methane in water under different pressures.

(2012) are adopted at the temperature in this paper, as shown in Table 4.

Subsequently, the amount of gas dissolved in water can be calculated as follows:

$$n_{sol} = \frac{x_g n_w}{(1 - x_g) m_m} = \frac{p_g n_w}{[a + (b-1) p_g + c p_g^2] m_m} \tag{15}$$

where n_{sol} denotes the amount of gas dissolved in water per unit mass, mmol/g; n_w represents the amount of water in the moist sample, mmol; m_m is the quality of moist sample, g.

Fig. 10 presents the dissolution curve of methane in water under reservoir conditions. It can be inferred that the dissolution amount of methane in water has an approximate linear relationship with pressure. Therefore, it is possible that the sum of methane adsorption and dissolution quantity of moist samples exceeds that of dry samples under higher pressure.

4.3 Adsorption model analysis for argillaceous silt

Among the models describing gas-solid isothermal adsorption, the most common one is the Langmuir model, which assumes that gas exhibits monolayer adsorption with the following assumptions: (1) the solid surface is homogeneous and there is no interaction between adjacent molecules; (2) the adsorption is located adsorption, and each adsorption site can only hold one adsorbent molecule (Duong, 1998). The Langmuir model is derived from statistical thermodynamics and is expressed as follows:
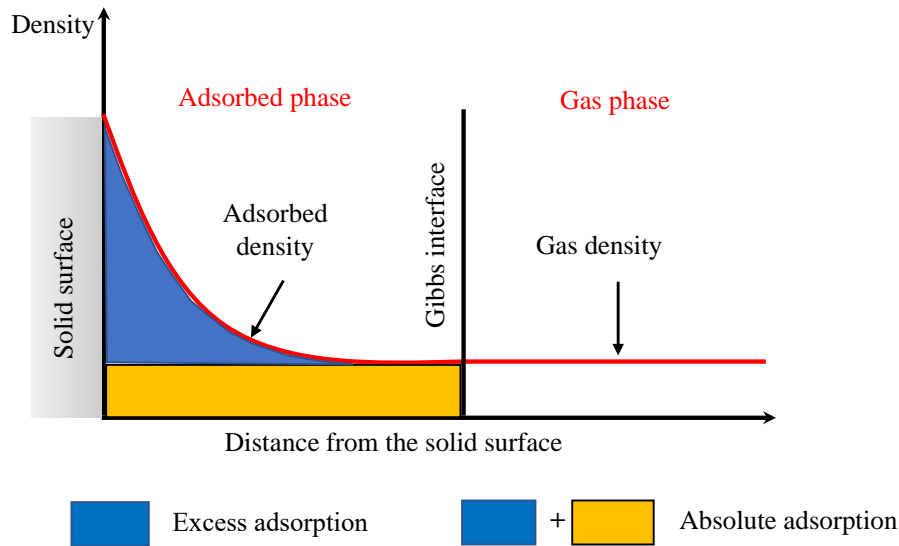
Fig. 11. Schematic diagram of excess and absolute adsorption capacity (modified from Clarkson and Haghshenas (2013)).

$$n_a = n_L \frac{p_g}{p_g + p_L} \tag{16}$$

where n_a denotes the absolute adsorption amount of solid per unit mass, mmol/g; n_L is Langmuir adsorption capacity, representing the maximum adsorption capacity, mmol/g; p_L refers to Langmuir pressure, defined as the pressure corresponding to half of the maximum adsorption capacity, MPa. The parameter p_L mainly affects the curvature of isothermal adsorption curve. The larger p_L, the gentler the adsorption curve.

However, in 1966, Dubinin presented experimental evidence of the fact that the adsorption mechanism was micropore filling. Through experiments, he demonstrated that the theoretical monolayer adsorption capacity of different zeolite samples was 2~3 times larger than that measured experimentally, and the ratio of experimental adsorption capacity to pore volume of different zeolite samples was the same (Dubinin, 1966). Therefore, Dubinin considered that the adsorption mechanism was micropore filling and established the Dubinin-Radushevich (D-R) micropore filling model, which has the following expression:

$$n_a = n_0 \exp \left[-D \left(\ln \frac{p_0}{p_g} \right)^2 \right] \tag{17}$$

where n_0 is the maximum adsorption capacity, corresponding to the microporous volume, mmol/g; D denotes a constant related to the adsorption affinity coefficient.

It should be pointed out that the experimentally measured adsorption capacity is excess adsorption capacity, and absolute adsorption capacity is the most common in practical application. Absolute adsorption capacity refers to the total amount of gas in the adsorbed phase, while excess adsorption capacity stands for the absolute adsorption capacity minus the amount of free gas in the adsorbed phase. The schematic diagram of the difference between the two is presented in Fig. 11. According to the definition of excess adsorption capacity and absolute adsorption capacity, it can be established that:

$$n_a = n_e + \rho_g V_a \tag{18}$$

In addition,

$$n_a = \rho_a V_a \tag{19}$$

The relationship between excess and absolute adsorption capacity can be obtained by combining Eqs. (18) and (19):

$$n_e = \left(1 - \frac{\rho_g}{\rho_a} \right) n_a \tag{20}$$

where n_e is excess adsorption capacity, mmol/g; ρ_g stands for the gas density, g/cm^3; ρ_a is the adsorbed phase density, g/cm^3; V_a refers to the adsorbed phase volume, cm^3.

Accordingly, on the basis of Langmuir and DR equations, by adding a correction factor $(1-\rho_g/\rho_a)$, the expression of excess adsorption capacity can be obtained:

$$n_e = n_L \left(1 - \frac{\rho_g}{\rho_a} \right) \frac{p_g}{p_g + p_L} \tag{21}$$

$$n_e = n_0 \left(1 - \frac{\rho_g}{\rho_a} \right) \exp \left[-D \left(\ln \frac{p_0}{p_g} \right)^2 \right] \tag{22}$$

Since there is no adsorption limit at low pressure, that is, reasonable n_L and n_0 values cannot be obtained, Kapoor et al. (1989) and Sakurovs et al. (2007) introduced the Henry constant into the equation to describe adsorption at low pressure. Besides, Sakurovs et al. (2007) modified the Langmuir and DR equations by using gas density instead of pressure, so that they could be used for supercritical adsorption. Based on the above description, the modified Langmuir and DR equations can be re-expressed as follows:

$$n_e = n_L \left(1 - \frac{\rho_g}{\rho_a} \right) \frac{\rho_g}{\rho_g + \rho_L} + k_H \rho_g \tag{23}$$

$$n_e = n_0 \left(1 - \frac{\rho_g}{\rho_a} \right) \exp \left[-D \left(\ln \frac{p_a}{p_g} \right)^2 \right] + k_H \rho_g \tag{24}$$
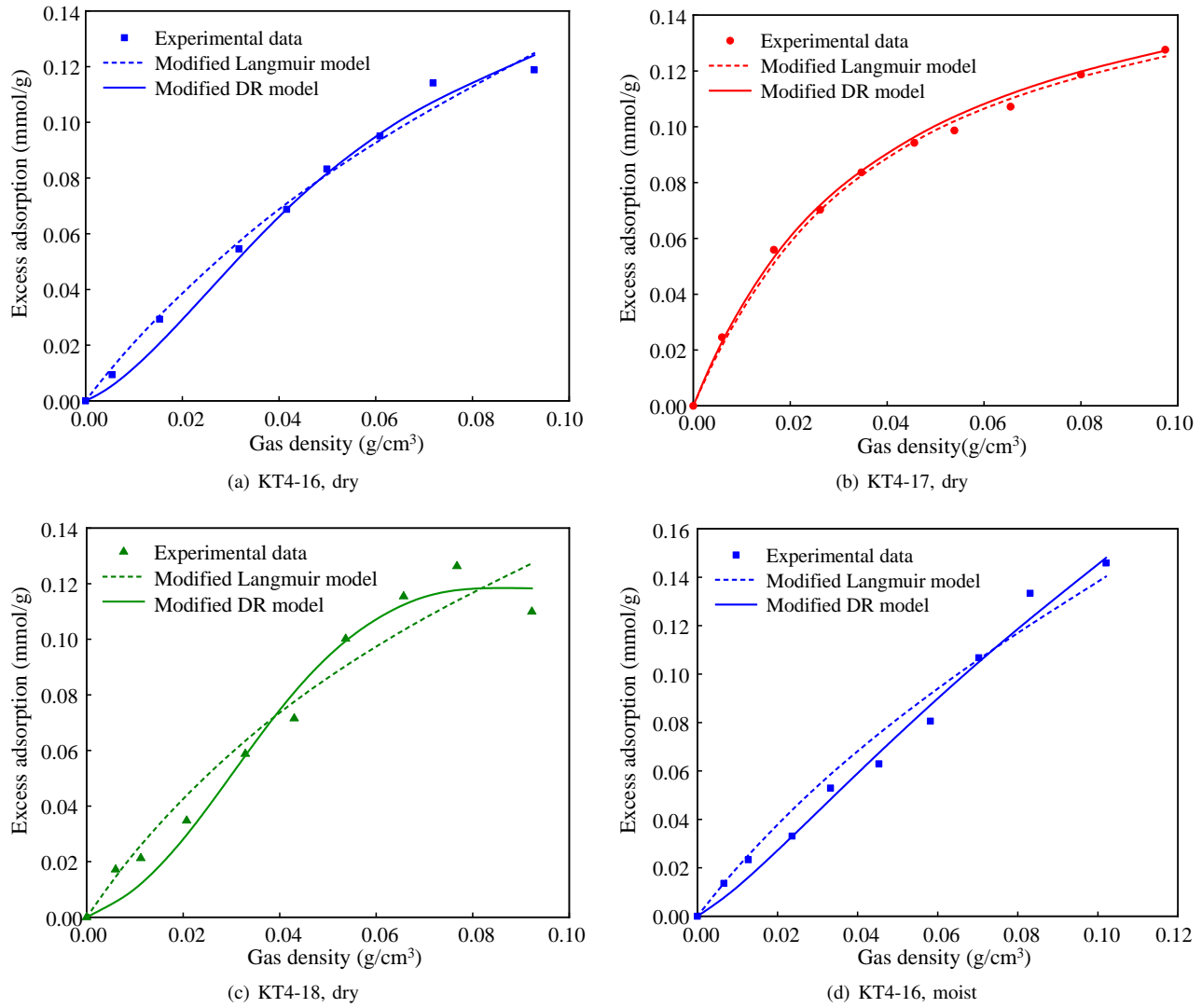
where ρ_L indicates Langmuir gas density, g/cm^3; k_H is Henry's

Fig. 12. Simulation results of the modified Langmuir and DR models.

constant, mmol·cm^3/g^2.

Then, the modified Langmuir and DR equations were used to fit the adsorption data, respectively, and the fitting results were shown in Fig. 12 and Table 4. The fitting effect was characterized by the average absolute deviation (AAD):

$$AAD = \left(\sum_{i=1}^{N} \frac{n_{ei}^c - n_{ei}^e}{n_{ei}^e N} \right) \times 100\% \qquad (25)$$

where N denotes the number of adsorption equilibrium; n_{ei}^c and n_{ei}^e are the simulated and experimental value at i^{th} equilibrium point, respectively, mmol/g.

As can be seen from Fig. 12 and Table 5, the fitting effect of the modified DR model is better than that of the modified Langmuir model. Comparing the two models, the Langmuir model is more suitable for simulating isothermal adsorption under lower pressure, while the modified DR equation is better for representing isothermal adsorption under medium and high pressure. This indicates that, in hydrate reservoirs, methane gas tends to adsorb on the surface when the pressure is low.

However, as the pressure increases, the adsorption sites on the surface gradually decrease, and methane gas fills into micropores instead. The order of the maximum adsorption capacity (n_L in Langmuir model and n_0 in DR equation) is basically consistent with the position of the adsorption curve in Fig. 6, which shows that the adsorption capacity of KT4-17 is the strongest, followed by KT4-18 and KT4-16. Compared with the dry sample, the Langmuir adsorption capacity n_L of the sample with 20% moisture content decreases by 21.88%, and the maximum adsorption capacity n_0 of DR decreases by 13.67%. According to publicly available experimental data, the presence of water in shale can reduce methane adsorption by 60%~90% (Gasparik et al., 2013; Merkel et al., 2015). Accordingly, the effect of water on methane adsorption in hydrate reservoir is much lower than that in shale, which may be due to the different sensitivities of mineral components to water. A study from Hatch et al. (2012) showed that there were some differences in the adsorption behavior of water on different types of clays. The outer surfaces of illite and montmorillonite were dominated by tetrahedral silica layers, while

Table 5. Fitting parameters of the modified Langmuir and DR models.

Model	Sample ID	n_L (mmol/g)	ρ_a (g/cm^3)	ρ_L (g/cm^3)	k_H (mmol·cm^3/g^2)	AAD (%)
	KT4-16, dry	0.128	0.491	0.080	0.745	4.62
	KT4-17, dry	0.165	0.341	0.041	0.434	2.63
Modified Langmuir	KT4-18, dry	0.160	0.520	0.080	0.616	10.48
	KT4-16, moist	0.100	0.443	0.080	0.952	9.87

Model	Sample ID	n_0 (mmol/g)	ρ_a (g/cm^3)	D	k_H (mmol·cm^3/g^2)	AAD (%)
	KT4-16, dry	0.139	0.215	0.375	0.689	7.22
	KT4-17, dry	0.171	0.543	0.097	0.225	2.33
Modified DR	KT4-18, dry	0.167	0.121	0.835	0.878	5.13
	KT4-16, moist	0.120	0.554	0.249	0.980	5.87

kaolinite had both alumina and silica layers. When the water content is small, for the three types of clay, water absorption is dominated by external surface adsorption. However, when the moisture content reaches a certain level, the water absorption of montmorillonite is mainly controlled by capillary adsorption in the pore network.

5. Conclusions

With the aim to verify the necessity of considering gas adsorption in hydrate reservoirs, this paper conducted exploratory experiments on the characterization of pore structure and the isothermal adsorption characteristics of argillaceous silt in the South China Sea, and compared the experimental results with those of shale. The main conclusions are as follows:

1) The pores of argillaceous silt are non-uniform slit pores formed by the accumulation of lamellar particles. The pore sizes are distributed from micropores to mesopores and macropores. The BET specific surface area is about 12 m^2/g, which is slightly smaller than that of shale from the Wufeng and Longmaxi Formations in the Sichuan Basin. As for the nanopore size range, the average pore size of argillaceous silt is 13.59~19.85 nm, which is 3~5 times that of shale.

2) Adsorption is a spontaneous exothermic reaction. Since the temperature of hydrate reservoir is much lower than that of shale reservoir, the gas adsorption magnitude of hydrate reservoir may be similar to that of shale reservoir. Therefore, the influence of gas adsorption should be considered in the process of hydrate exploitation.

3) The influence of water on methane adsorption can be divided into three parts: at low pressure (<2 MPa), the water content has little effect on methane adsorption; under medium pressure (2~10 MPa), the methane adsorption capacity is reduced by the water content; at higher pressure (>10 MPa), the adsorption capacity of the sample increases with the water content. The promotive effect of moisture on methane adsorption under high pressure may be due to the dissolution of methane in water.

4) Compared with dry argillaceous silt, when the moisture content is 20%, the Langmuir adsorption capacity nL decreases by 21.88%, and the maximum adsorption capacity n0 of DR decreases by 13.67%, both of which are far lower than the influence of water on shale. This may be due to the low sensitivity of mineral components in argillaceous silt to water.

Conflict of interest

The authors declare no competing interest.

References

Barrett, E. P., Joyner, L. G., Halenda, P. P., et al. The determination of pore volume and area distributions in porous substances. I. Computations from nitrogen isotherms. Journal of the American Chemical Society, 1951, 73(1): 373-380.

Busch, A., Gensterblum, Y. CBM and CO$_2$-ECBM related sorption processes in coal: A review. International Journal of Coal Geology, 2011, 87(2): 49-71.

Carty, R. Thermodynamic properties of helium 4 from 2 to 1500 K at pressures to 108 Pa. United States, National Bureau of Standards, 1973.

Chalmers, G. R. L., Bustin, R. M. The organic matter distribution and methane capacity of the Lower Cretaceous strata of Northeastern British Columbia, Canada. International Journal of Coal Geology, 2007, 70(1/3): 223-239.

Chareonsuppanimit, P., Mohammad, S. A., Robinson, R. L., et al. High-pressure adsorption of gases on shales: Measurements and modeling. International Journal of Coal Geology, 2012, 95: 34-46.

Chareonsuppanimit, P., Mohammad, S. A., Robinson, R. L., et al. Modeling the temperature dependence of supercritical gas adsorption on activated carbons, coals and shales. International Journal of Coal Geology, 2015, 138: 113-126.

Clarkson, C., Haghshenas, B. Modeling of supercritical fluid adsorption on organic-rich shales and coal. Paper SPE-164532-MS Presented at Society of Petroleum Engineers - SPE USA Unconventional Resources Conference, The Woodlands, Texas, 10-12 April, 2013.

Dubinin, M. Porous structure and adsorption properties of active carbons. Chemistry and Physics of Carbon, 1966, 9: 51-119.

Dubinin, M., Astakhov, V. Development of the concepts of volume filling of micropores in the adsorption of gases and vapors by microporous adsorbents. Physical Chemistry, 1971, 20: 8-12.

Duong, D. D. Adsorption analysis: Equilibria and kinetics. Chemical Engineer Series. 1998, 2: 49-77.

Fletcher, A. J., Thomas, K. M., Rosseinsky, M. J. Flexibility in metal-organic framework materials: Impact on sorption properties. Journal of Solid State Chemistry, 2005, 178(8): 2491-2510.

Gasparik, M., Ghanizadeh, A., Bertier, P., et al. High-pressure methane sorption isotherms of black shales from the Netherlands. Energy & Fuels, 2012, 26(8): 4995-5004.

Gasparik, M., Ghanizadeh, A., Gensterblum, Y., et al. "Multi-temperature" method for high-pressure sorption measurements on moist shales. Review of Scientific Instruments, 2013, 84(8): 085116.

Groen, J. C., Peffer, L. A. A., Pérez-RamíRez, J. Pore size determination in modified micro- and mesoporous materials. Pitfalls and limitations in gas adsorption data analysis. Microporous and Mesoporous Materials, 2003, 60(1): 1-17.

Gurvitsch, L. Physicochemical attractive force. Russian Journal of Physical Chemistry, 1915, 47: 805-827.

Hatch, C. D., Wiese, J. S., Crane, C. C., et al. Water adsorption on clay minerals as a function of relative humidity: Application of BET and freundlich adsorption models. Langmuir, 2012, 28: 1790-1803.

Ji, L., Zhang, T., Milliken, K., et al. Experimental investigation of main controls to methane adsorption in clay-rich rocks. Applied Geochemistry, 2012, 27(12): 2533-2545.

Kapoor, A., Ritter, J. A., Yang, R. T. On the Dubinin-Radushkevich equation for adsorption in microporous solids in the Henry's law region. Langmuir, 1989, 5(4): 1118-1121.

Li, J., Ye, J., Qin, X., et al. The first offshore natural gas hydrate production test in South China Sea. China Geology, 2018, 1: 5-16.

Li, Y., Li, X., Wang, Y., et al. Effects of composition and pore structure on the reservoir gas capacity of Carboniferous shale from Qaidam Basin, China. Marine and Petroleum Geology, 2015, 62: 44-57.

Liu, B., Gao, Y., Liu, K., et al. Pore structure and adsorption hysteresis of the middle Jurassic Xishanyao shale formation in the Southern Junggar Basin, northwest China. Energy Exploration & Exploitation, 2021a, 39: 761-778.

Liu, B., Sun, J., Zhang, Y., et al. Reservoir space and enrichment model of shale oil in the first member of Cretaceous Qingshankou Formation in the Changling sag, southern Songliao Basin, NE China. Petroleum Exploration and Development, 2021b, 48(3): 608-624.

Liu, C., Meng, Q., He, X., et al. Characterization of natural gas hydrate recovered from Pearl River Mouth basin in South China Sea. Marine and Petroleum Geology, 2015, 61(61): 14-21.

Liu, D., Yuan, P., Liu, H., et al. High-pressure adsorption of methane on montmorillonite, kaolinite and illite. Applied Clay Science, 2013, 85: 25-30.

Lu, X., Li, F., Watson, A. T. Adsorption measurements in Devonian shales. Fuel, 1995, 74(4): 599-603.

Luo, X., Wang, S., Wang, Z., et al. Adsorption of methane, carbon dioxide and their binary mixtures on Jurassic shale from the Qaidam Basin in China. International Journal of Coal Geology, 2015, 150-151: 210-223.

Marsh, H. Adsorption methods to study microporosity in coals and carbons—a critique. Carbon, 1987, 25(1): 49-58.

Merkel, A., Fink, R., Littke, R. The role of pre-adsorbed water on methane sorption capacity of Bossier and Haynesville shales. International Journal of Coal Geology, 2015, 147-148(1): 1-8.

Mohammadi, M. R., Bahmaninia, H., Ansari, S., et al. Evaluation of asphaltene adsorption on minerals of dolomite and sandstone formations in two and three-phase systems. Advances in Geo-Energy Research, 2021, 5(1): 39-52.

Myers, A. L., Monson, P. A. Adsorption in porous materials at high pressure: Theory and experiment. Langmuir, 2002, 18: 10261-10273.

Polanyi, M. Adsorption from the point of view of the Third Law of Thermodynamics. Deutsch Physics, 1914, 16: 1012-1016.

Qi, R. Study on multi-component competitive adsorption mechanism of shale gas. China University of Petroleum, Beijing, 2019. (in Chinese)

Qi, R., Ning, Z., Wang, Q., et al. Measurements and modeling of high-pressure adsorption of CH_4 and CO_2 on shales. Fuel, 2019, 242(9): 728-743.

Qi, R., Ning, Z., Wang, Q., et al. Sorption of methane, carbon dioxide, and their mixtures on shales from Sichuan Basin, China. Energy & Fuels, 2018, 32(3): 2926-2940.

Qin, X., Lu, J., Lu, H., et al. Coexistence of natural gas hydrate, free gas and water in the gas hydrate system in the Shenhu Area, South China Sea. China Geology, 2020, 3: 210-220.

Rexer, T. F. T., Benham, M. J., Aplin, A. C. et al., Methane adsorption on shale under simulated geological temperature

and pressure conditions. Energy & Fuels, 2013, 27(6): 3099-3109.

Ross, D. J. K., Bustin, R. M. Shale gas potential of the Lower Jurassic Gordondale Member, northeastern British Columbia, Canada. Bulletin of Canadian Petroleum Geology, 2007, 55(1): 51-75.

Ross, D. J. K., Bustin, R. The importance of shale composition and pore structure upon gas storage potential of shale gas reservoirs. Marine and Petroleum Geology, 2009, 26(6): 916-927.

Rouquerol, J., Avnir, D., Fairbridge, C. W., et al. Recommendations for the Characterization of Porous Solids. Pure and Applied Chemistry, 1994, 66(8): 1739-1758.

Ruppel, C. D., Kessler, J. D. The interaction of climate change and methane hydrates. Reviews of Geophysics, 2016, 55(1): 126-168.

Sakurovs, R., Day, S.,Weir, S., et al. Application of a modified Dubinin-Radushkevich equation to adsorption of gases by coals under supercritical conditions. Energy & Fuels, 2007, 21(2): 992-997.

Schettler, P., Parmely, C. Contributions to total storage capacity in Devonian Shales. Paper SPE-23422-MS Presented at the SPE Eastern Regional Meeting, Lexington, Kentucky, 22-25 October, 1991.

Setzmann, U., Wagner, W. A new equation of state and tables of thermodynamic properties for methane covering the range from the melting line to 625 K at pressures up to 100 MPa. Journal of Physical and Chemical Reference Data, 1991, 20(6): 1061-1155.

Shaibu, R., Sambo, C., Guo, B., et al. An assessment of methane gas production from natural gas hydrates: Challenges, technology and market outlook. Advances in Geo-Energy Research, 2021, 5(3): 318-332.

Shen, W., Li, X., Cihan, A., et al. Experimental and numerical simulation of water adsorption and diffusion in shale gas reservoir rocks. Advances in Geo-Energy Research, 2019, 3(2): 165-174.

Sing, K. S. Reporting physisorption data for gas/solid systems with special reference to the determination of surface area and porosity. Pure and Applied Chemistry, 1985, 57(4): 603-619.

Wang, Y., Yu, Q. The effect of moisture on the methane adsorption capacity of shales: A study case in the eastern Qaidam Basin in China. Journal of Hydrology, 2016, 542: 487-505.

Yang, F., Xie, C., Ning, Z., et al. High-pressure methane sorption on dry and moisture-equilibrated shale. Energy & Fuels, 2017a, 31: 482-492.

Yang, F., Xie, C., Xu, S., et al. Supercritical methane sorption on organic-rich shales over a wide temperature range. Energy & Fuels, 2017b, 31: 13427-13438.

Ye, J., Qin, X., Xie, W., et al. The second natural gas hydrate production test in the South China Sea. China Geology, 2020, 3: 197-209.

Zhang, C., Zhou, S., Li, J., et al. Adsorption characteristics of CH_4 and CO_2 on shale and its application to binary mixture adsorption under high-pressure conditions: A case study of the Longmaxi Formation shale in Jiaoshiba area of Sichuan Basin. Geochimica, 2019, 48(6): 580-589. (in Chinese)

Zhang, T., Ellis, G. S., Ruppel, S. C., et al. Effect of organic-matter type and thermal maturity on methane adsorption in shale-gas systems. Organic Geochemistry, 2012, 47: 120-131.

Zhou, S., Ning, Y., Wang, H., et al. Investigation of methane adsorption mechanism on Longmaxi shale by combining the micropore filling and monolayer coverage theories. Advances in Geo-Energy Research, 2018, 2(3): 269-281.

Zhou, Y. P., Zhou, L. Fundamentals of high pressure adsorption. Langmuir, 2009, 25: 13461-13466.

Zhu, H., Ju, Y., Huang, C., et al. Microcosmic gas adsorption mechanism on clay-organic nanocomposites in a marine shale. Energy, 2020, 197: 117256.

Zhu, H., Ju, Y., Qi, Y., et al. Impact of tectonism on pore type and pore structure evolution in organic-rich shale: Implications for gas storage and migration pathways in naturally deformed rocks. Fuel, 2018, 228: 272-289.